PHYSICAL REVIEW B VOLUME 36, NUMBER 9 15 SEPTEMBER 1987-II

Angle-resolved photoemission study of the electronic band structure of the ZrC(100) surface

P. A. P. Lindberg, P. L. Wincott, and L. I. Johansson
Department of Physics and Measurement Technology, Linköping University, S-581 83 Linköping, Sweden

A. N. Christensen
Department of Chemistry, Aarhus University, DK-8000 Aarhus C, Denmark

(Received 25 March 1987)

The energy-band structure of $ZrC_{0.92}$ has been investigated utilizing angle-resolved photoelectron spectroscopy. Energy distribution curves from the (100) surface were recorded along both the $\langle 010 \rangle$ and the $\langle 011 \rangle$ symmetry directions using He I, Ne I, and Ar I resonance radiation. The experimental data are compared with the band structure of $ZrC_{1.0}$ calculated using the linear augmented-plane-wave method. Theoretical energy-distribution curves for $ZrC_{1.0}$ are also presented and used for the interpretation of the experimental results. A good agreement between experimental and theoretical peak dispersions and intensity variations is found, showing that most of the structures observed in the experimental spectra are well accounted for by direct bulk energy-band transitions. A three-dimensional density-of-states feature is observed at about -3 eV at large emission angles in the Ar I–induced recorded spectra.

I. INTRODUCTION

The transition-metal nitrides and carbides (TMNC's) have been the object of both practical and theoretical interest during the past years. Because of their ultrahardness and high melting point they have found application as high-temperature structural materials and wear-resistant coatings. In addition to these properties that are characteristic of strongly covalently bonded crystals, they also exhibit metallic conductivity, and some of them show very promising superconducting properties.[1]

On the theoretical side, the large interest for the TMNC's is mainly due to their unusual combination of bonding mechanisms, involving covalent, ionic, and metallic bonding, which are believed to account for the unique combination of macroscopic properties that this group of materials displays. In view of this, much attention has been focused on the electronic band structure and bonding mechanisms of these compounds, aiming at obtaining an understanding of their physical properties. The theoretical treatment of stoichiometric compounds of the TMNC's is fairly simple, since they crystallize in the well-known rock salt structure. However, real samples contain, in general, a large amount of vacancies primarily in the nonmetal sublattice. The vacancies are of crucial importance for the macroscopic properties. The resistivity, magnetic susceptibility, and superconducting properties are, for example, all strongly changed by the introduction of vacancies.[1]

In this study the electronic band structure of the (100) surface of $ZrC_{0.92}$ has been investigated using angle-resolved photoelectron spectroscopy. Energy distribution curves (EDC's) were recorded along both the $\langle 010 \rangle$ and the $\langle 011 \rangle$ symmetry directions using three different photon energies, He I (21.2 eV), Ne I (16.8 eV), and Ar I (11.8 eV). The energy-band structure of $ZrC_{1.0}$, calculated using the linear augmented-plane-wave (LAPW) method, is used for interpreting the normal-emission data. The recorded EDC's are also compared with calculated spectra for $ZrC_{1.0}$, using an extended version[2] of Pendry's model[3] for photoemission. The calculated spectra give information on both the peak locations and transition probabilities, thus enabling the experimental peak dispersions as well as the relative peak intensities to be compared with the theoretical predictions. The results show that most of the structures observed in the experimental spectra are well explained in terms of direct bulk energy-band transitions. Emission from a three-dimensional density of states feature is observed at large emission angles in the Ar I–induced spectra.

II. EXPERIMENTAL AND THEORETICAL DETAILS

A. Experiment

Angle-resolved-photoemission measurements have been performed using unpolarized resonance radiation from a conventional-discharge uv lamp. The resonance lines used were He I, Ne I, and Ar I, providing radiation with energy 21.2 eV, 16.8 eV, and 11.8 eV, respectively. The experiments were carried out in a VG ADES 400 photoemission system operating at a base pressure of less than 1×10^{-10} Torr. The photoemitted electrons were analyzed with respect to their kinetic energy and direction of propagation using a movable hemispherical electrostatic analyzer. The analyzer had an acceptance cone of ±2° and was operating at an energy resolution of 0.2 eV.

Single crystals of ZrC_x were grown using a vertical floating-zone technique.[4] The composition of the crystal, $ZrC_{0.92}$, was determined by chemical analysis.[5] The crystal was mounted in the photoemission system with the surface perpendicular to the analyzer plane within ±1°. It was cleaned *in situ* by repeated flash heatings to about 1600 °C. Prior to measurements, the order and the cleanliness of the surface were examined using low-energy electron diffraction (LEED) and ultraviolet photoemission spectroscopy (UPS). A sharp, well-ordered 1×1 LEED pattern was observed, and no sign of contamination peaks could be seen in the UPS spectra. To keep the surface clean during the measurements, high-temperature flashings to about 1600 °C were performed every fourth hour.

In the spectra presented below, the electron energies are referred to the midpoint of the Fermi edge, and both the incidence angle of the radiation, θ_i, and the emission angle of the electrons, θ_e, are given relative to the crystal surface normal.

B. Band-structure calculation

The electronic band structure of $ZrC_{1.0}$ has been calculated using the nonrelativistic self-consistent linear augmented-plane-wave method.[6] The band-structure calculation was performed in two steps. Firstly, a self-consistent potential was generated by calculating the charge density at ten special **k** points[7] in $\frac{1}{48}$ of the Brillouin zone. The wave functions of both the core and the valence electrons were recalculated in each iteration cycle, and self-consistency was carried out until the energy eigenvalues were stable within about 1 mRy. Nonspherical contributions to the potential were approximately taken account of by extending the wave function in the interstitial region into the muffin-tin spheres. In the second step the energy-band structure was obtained by calculating the energy eigenvalues on a relatively fine k mesh, dividing the $\Gamma \rightarrow X$ symmetry line into 32 equally spaced intervals. Since the linearization in the LAPW method gives accurate eigenvalues over an energy region of about 1 Ry, the energy range of interest was divided into four parts. The energy values, E_l, around which the radial wave functions are expanded are given in Table I. By combining the energy eigenvalues in the four different energy regions, the complete band structure of $ZrC_{1.0}$ (see Fig. 1) was obtained.

In the calculations the first nine spherical harmonics were used in the expansion of the wave function inside the muffin-tin spheres, and the wave function in the interstitial region was represented by a linear combination of unsymmetrized plane waves. The number of plane waves used was 89 for generating the self-consistent potential and 113 for the actual band-structure calculations. The calculations were performed within the local-density-functional (LDF) formalism[8] and the Hedin-Lundquist approximation[9] was used to take account of the exchange and correlation potential. No effort has been made to correct for relativistic effects, since these have been shown[10] to be small for the refractory carbides of the second-row transition metals.

TABLE I. Energy parameters E_l for the LAPW calculation. All energies (in Ry) are given relative to the muffin-tin zero. (The Fermi energy E_F is located at 0.708 Ry.) See Sec. II B for details.

Region	E_l
1	C sphere: $E_l=0.5$ Ry, except $E_0=-0.05$ Ry, $E_1=0.40$ Ry Zr sphere: $E_l=0.5$ Ry, except $E_1=1.8$ Ry, $E_2=0.45$ Ry
2	C sphere: $E_l=1.3$ Ry Zr sphere: $E_l=1.3$ Ry, except $E_1=2.0$ Ry
3	All $E_l=2.2$ Ry
4	All $E_l=3.2$ Ry

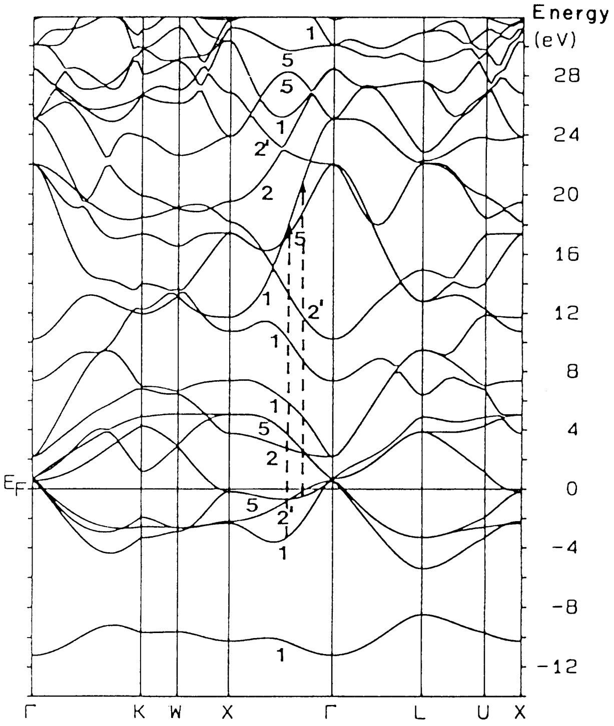

FIG. 1. Energy-band structure of $ZrC_{1.0}$ calculated using the LAPW method. Direct transitions for 21.2-eV radiation at normal emission from the (100) surface are indicated by the dashed arrows. The symmetries of the energy bands are given along the $\Gamma \rightarrow X$ symmetry line.

Since the experimental normal emission data allow a direct comparison with the calculated band structure along the Δ direction, we are primarily interested in the symmetries of the energy bands along this symmetry direction. In Fig. 1 the irreducible representations to which the energy bands belong have therefore been indicated along this $\Gamma \rightarrow X$ symmetry line.

C. Calculated spectra

The extension of the time-reversed LEED theory[3] to include ordered binary compounds[2] has previously been successfully applied to calculate the photocurrent from the (100) face of transition-metal carbides and nitrides.[11,12] In this study the extended version is utilized to calculate angle-resolved photoemission spectra from ZrC(100).

Ideal crystal conditions were assumed in the calculations. This means that the self-consistent muffin-tin potentials, generated for the band-structure calculation of

$ZrC_{1.0}$, described above, were used in all layers, and that bulk atomic positions were assumed also at the surface. Hence, the calculated spectra essentially reflect the bulk energy-band structure of stoichiometric ZrC. A steplike potential barrier was used at the solid-vacuum interface. The barrier was positioned immediately outside the muffin-tin sphere radii of the Zr atoms in the top layer, and its height was determined from the measured work function. In accordance with earlier calculations[11,12] on the transition-metal nitrides and carbides, the imaginary parts of the potential were chosen to be -0.14 and -2.0 eV for the low- and high-energy electron states, respectively. These values, although not optimized, have been shown[11,12] to reflect the widths of the experimental features fairly well. Unpolarized radiation was simulated in the calculations by rotating the electric field vector 45° with respect to the analyzer plane. This does not give a true description of the electromagnetic field, but since neither reflection nor refraction at the surface has been taken account of, we use this simple model as an appropriate approximation. To obtain convergence 21 reciprocal-lattice vectors were used in the calculations.

In the calculated spectra shown below, only relative intensities within each photoemission spectrum should be compared, since no effort has been made to correct for optical effects at the surface. The spectra have not been convoluted with the Fermi-Dirac electron distribution function and consequently the Fermi energy is not explicitly marked out.

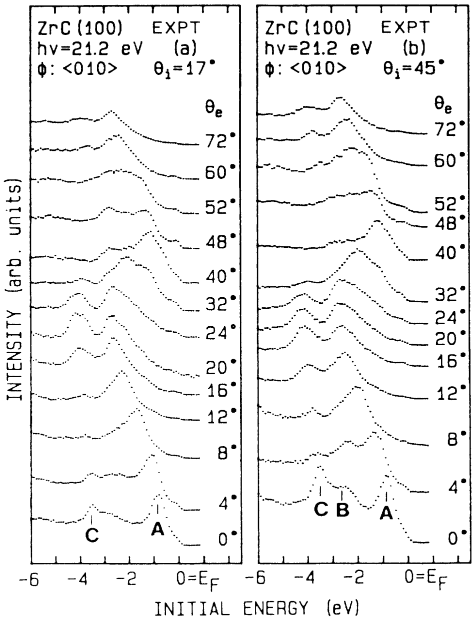

FIG. 2. Experimental angle-resolved EDC's from ZrC(100) using He I (21.2 eV) radiation and measured at various emission angles along the ⟨010⟩ azimuth. The incidence angle of the radiation is (a) $\theta_i = 17°$ and (b) $\theta_i = 45°$.

III. RESULTS AND DISCUSSION

A. The ⟨010⟩ azimuth

Experimental angle-resolved-energy distribution curves from ZrC(100) recorded at various emission angles along the ⟨010⟩ azimuth are shown in Fig. 2. The EDC's were induced by unpolarized He I (21.2 eV) radiation incident along the ⟨010⟩ azimuth at (a) $\theta_i = 17°$ and (b) $\theta_i = 45°$. At normal emission three prominent structures, labeled *A*, *B*, and *C*, appear. Clear polarization effects are seen when comparing the normal emission spectra measured at the two incidence angles. By increasing the incidence angle from $\theta_i = 17°$ to $\theta_i = 45°$, peak *A* is seen to become relatively weaker, while peaks *B* and *C* gain relative strength. Using the simple geometrical fact that the ratio between the perpendicular and the parallel component of the electric field increases monotonically with increasing incidence angle, the symmetry of the initial states can be determined by referring to photoemission selection rules.[13,14] These rules, applicable at normal emission, give that the perpendicular (parallel) component of the electric field vector can induce transitions from initial states of Δ_1 (Δ_5) symmetry to an allowed final state of Δ_1 symmetry. Hence, peaks *A* and *C* can unambiguously be attributed to transitions from initial states of Δ_5 and Δ_1 symmetry, respectively. The incidence angle dependence of peak *B*, although not as pronounced as for the other two peaks, suggests that it is due to initial states of Δ_1 symmetry. However, as will be discussed below, other effects may also contribute to the emission strength of peak *B*.

These assignments of the peaks observed in the normal emission spectra are in good agreement with the calculated band structure of $ZrC_{1.0}$ in Fig. 1. It is seen in Fig. 1 that along the $\Gamma \rightarrow X$ symmetry line the valence band between -5 eV and the Fermi level consists of three partially occupied energy bands. As mentioned above, emission from two of these bands, of Δ_1 and Δ_5 symmetry, is expected to be seen at normal emission, while emission from the $\Delta_{2'}$ band is forbidden by the symmetry selection rules. The dashed arrows in Fig. 1 indicate symmetry-allowed direct transitions for 21.2-eV radiation. By using the direct transition model we see that the initial-state bands of Δ_1 and Δ_5 symmetry are expected to give rise to two emission peaks around -3 and -0.5 eV, respectively, in accordance with the experimental findings for peaks *C* and *A*.

Returning to Fig. 2, we see that strong energy dispersions with the emission angle occur. Peak *A* moves rapidly with the emission angle; it shifts downwards, goes through an energy minimum at about $\theta_e = 20°$ and moves then back towards higher energies, until, around $\theta_e = 40°$, it again reverses its direction. Peak *C* shifts slowly, but systematically, towards lower energies and dies out almost completely at emission angles above $\theta_e = 40°$. At the larger emission angles, $\theta_e > 52°$, emission from a feature at about -4 eV can again be observed. Peak *B* is discernible only at the smaller emission angles, presumably due to overlap effects from peak *A*; at about $\theta_e = 8°$ these peaks merge and cannot be resolved from each other. It should also be noted that strong intensity variations occur, in particular for peak *C*, which around $\theta_e=20°$ exhibits a pronounced intensity maximum and is rapidly attenuated at larger emission angles.

Theoretical angle-resolved EDC's for 21.2-eV radiation calculated at different emission angles along the ⟨010⟩ azimuth are shown in Fig. 3. The incidence angles of the radiation are the same as those in the experimental spectra, i.e., $\theta_i=17°$ in Fig. 3(a) and $\theta_i=45°$ in Fig. 3(b). The overall agreement between the experimental and theoretical spectra is found to be very good. At normal emission, clear polarization effects are seen, justifying the assignments made above for the peaks observed in the normal-emission experimental spectra. The Δ_1 structure is considerably broader than the Δ_5 peak, mainly due to the fact that the Δ_1 band is much steeper than the Δ_5 band, see Fig. 1. Considering that the Δ_1 structure has an appreciable emission strength between about -2 and -4 eV, direct transitions from initial states of Δ_1 symmetry may very well account for both peaks *B* and *C*. Indeed, a closer examination of the Δ_1-derived structure at $\theta_e=4°$ clearly reveals a peak at about -2.5 eV. The dispersions of the experimental peaks are also well reflected by the calculations. A Δ_5-derived peak reproduces the strong dispersion of peak *A* in the recorded spectra fairly well, and the behavior of peak *C* is mimicked by the Δ_1-derived structure in the calculated spectra. In accordance with the experimental data, a strong emission feature comes up around -1 eV at about $\theta_e=20°$, and at the larger emission angles a structure appears between -3 and -4 eV. In addition, the intensity variations of the spectral features in the experimental and theoretical spectra agree satisfactorily. In both the recorded and calculated spectra the Δ_1-derived structure is seen to go through a pronounced intensity maximum around $\theta_e=20°$, while at intermediate emission angles, between $\theta_e=30°$ and $\theta_e=40°$, the spectra are dominated by the two highest-lying structures. There is also a rather good agreement concerning absolute peak locations. In general, the calculated structures are located about 0.5 eV closer to the Fermi energy. However, considering that much larger discrepancies between the experimental and calculated peak positions, especially for the Δ_5 structure, have been observed previously on other transition-metal nitrides and carbides,[15–17] a disagreement in peak positions of only about 0.5 eV is very encouraging.

Experimental EDC's excited by unpolarized Ne I (16.8 eV) radiation and measured at different emission angles along the ⟨010⟩ azimuth are shown in Fig. 4. Again, three peaks are observed at normal emission. As compared with the He I–induced spectra, the polarization effects appear more clearly at this photon energy. Peak *C* is dramatically attenuated by decreasing the incidence angle from $\theta_i=45°$ to $\theta_i=17°$, while peak *B* is less affected. Moreover, the relative emission intensity of peak *A* is higher at the smaller incidence angle, confirming its Δ_5 character. At the smaller emission angles, downward energy dispersions with the emission angle are observed for both peaks *A* and *C*. Peak *A* exhibits strong dispersion and starts overlapping peak *B* at $\theta_e=12°$. Peak *C* shifts slowly towards lower energies and becomes weaker. The spectra measured at $\theta_i=17°$

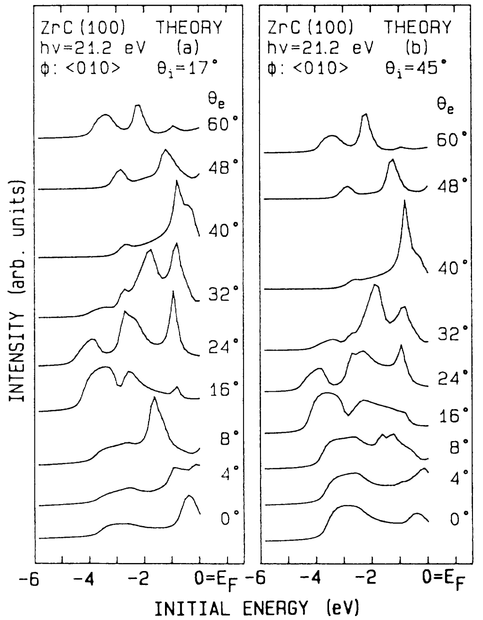

FIG. 3. Theoretical angle-resolved EDC's for ZrC(100) induced by 21.2-eV radiation and calculated at different emission angles along the ⟨010⟩ azimuth. The incidence angle of the radiation is (a) $\theta_i=17°$ and (b) $\theta_i=45°$.

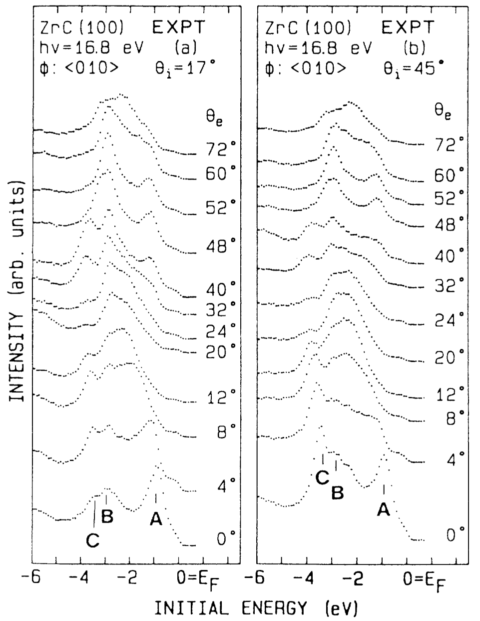

FIG. 4. Experimental angle-resolved EDC's from ZrC(100) using Ne I (16.8 eV) radiation and measured at various emission angles along the ⟨010⟩ azimuth. The incidence angle of the radiation is (a) $\theta_i=17°$ and (b) $\theta_i=45°$.

show that peak *B* is located around -3 eV almost independently of the emission angle. Above $\theta_e = 20°$, strong intensity modulations can be seen. The lowest-lying structure, which is hardly visible at $\theta_e = 20°$, becomes considerably stronger at larger emission angles and shifts upwards, approaching the main peak at about -3 eV. Furthermore, around $\theta_e = 40°$, a sharp peak comes up at about 1 eV binding energy. The emission strength of this peak increases systematically with the emission angle, until around $\theta_e = 50°$ it becomes broader and shifts slightly downwards.

Calculated angle-resolved EDC's simulating some of the Ne I–induced experimental EDC's are shown in Fig. 5. The observations made when comparing the experimental and calculated spectra for 21.2-eV radiation are further emphasized at this photon energy. The calculated spectra reproduce the dispersions of peaks *A* and *C* very well, and again we note that the absolute peak locations are, in general, slightly higher in the theoretical spectra. Moreover, the theoretical normal emission spectra calculated at $\theta_i = 45°$, clearly show that a shoulder appears at about -2.5 eV on the high-energy side of the Δ_1 emission structure. This shoulder is easily discernible at the smaller emission angles, until around $\theta_e = 20°$ overlap effects from the downward dispersing Δ_5-derived peak become too severe. Thus the theoretical results account fairly well for peak *B* in the experimental spectra, at least at the smaller emission angles. At emission angles above $\theta_e = 20°$, a sharp feature appears around -1 eV. It exhibits a pronounced intensity maximum at $\theta_e = 48°$ and moves slowly away from the Fermi energy, in accordance with the experimental findings. It should also be noted that the calculated spectra account fairly well for the intensity modulation of peak *C* in the experimental spectra, although at $\theta_e = 32°$ its relative strength is slightly higher in the experimental data.

Angle-resolved EDC's were also measured using unpolarized Ar I (11.8 eV) radiation, and, as will be shown below, the comparison between the experimental and calculated EDC's at $h\nu = 11.8$ eV is of crucial importance for sorting out structures in the experimental spectra that cannot be explained in terms of direct transitions. Figure 6 shows experimental EDC's induced by unpolarized Ar I radiation and recorded at various emission angles along the ⟨010⟩ azimuth. Two prominent structures are observed at the smaller emission angles. The uppermost is as before due to direct transitions from the bulk Δ_5 initial-state band, while the lower lying structure is attributed to emission from initial states of Δ_1 symmetry. Thus, in contrast to the spectra induced by Ne I and He I radiation, only one peak exhibiting Δ_1 symmetry appears. The reason for this becomes clear when examining the calculated band structure in Fig. 1. For Ar I (11.8 eV) radiation direct transitions may take place from the steep part of the Δ_1 initial-state band to a final-state band of Δ_1 symmetry located between 7 and 12 eV. Hence, compared with the Ne I and He I excited spectra, peak *C* in the normal emission spectra is expected to have shifted upwards to a position slightly above about -3 eV, prohibiting peaks *B* and *C* from being distinguished in the normal-emission spectra.

With increasing emission angle the two structures

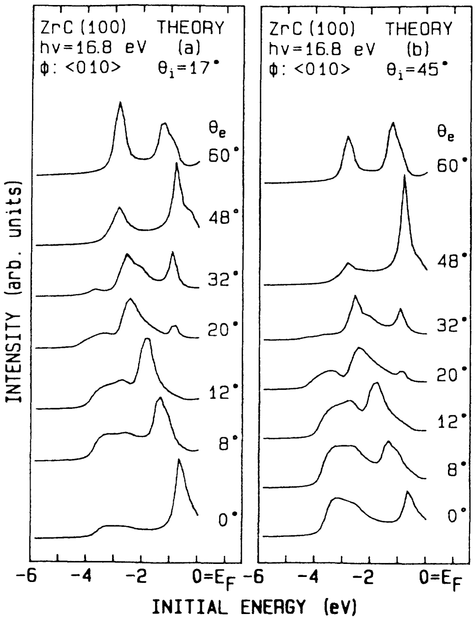

FIG. 5. Theoretical angle-resolved EDC's for ZrC(100) induced by 16.8-eV radiation and calculated at different emission angles along the ⟨010⟩ azimuth. The incidence angle of the radiation is (a) $\theta_i = 17°$ and (b) $\theta_i = 45°$.

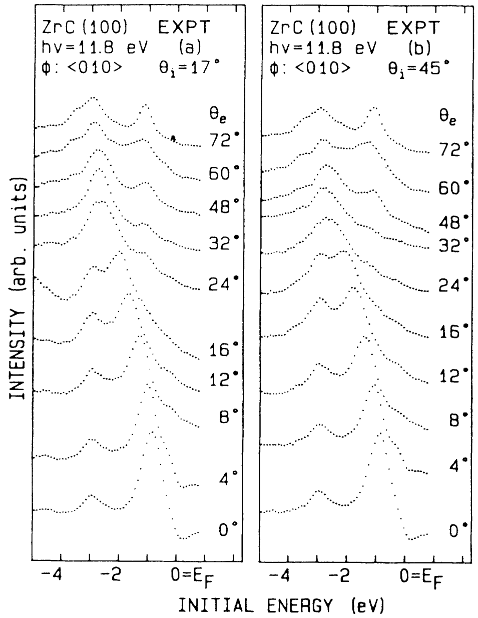

FIG. 6. Experimental angle-resolved EDC's from ZrC(100) using Ar I (11.8 eV) radiation and measured at various emission angles along the ⟨010⟩ azimuth. The incidence angle of the radiation is (a) $\theta_i = 17°$ and (b) $\theta_i = 45°$.

behave quite differently. While the lower-lying structure shows almost no dispersion with the emission angle, the Δ_5-derived peak shifts rapidly towards lower energies. At about $\theta_e = 30°$, the two structures merge and cannot be resolved from each other. At the larger emission angles, above $\theta_e = 20°$, a nondispersive structure appears at about 1-eV binding energy. We also note that at $\theta_e > 20°$ no or very little dispersion is observed for the main structure at -3 eV, and at the larger emission angles, a shoulder appears on its low-energy side.

Theoretical angle-resolved EDC's for 11.8-eV radiation calculated at various emission angles along the $\langle 010 \rangle$ azimuth are shown in Fig. 7. In accordance with the experimental results, two structures, which show strong dependence on the polarization of the radiation, are observed. Moreover, the absolute peak locations and peak dispersions agree satisfactorily with the experimental data. It is, in particular, encouraging to see how well the calculated spectra account for the nondispersive structure around -1 eV that is observed in the measured spectra at $\theta_e > 20°$. However, at $\theta_e = 72°$, a severe discrepancy between the experimental and calculated spectra occurs. At this angle, two prominent structures are observed in the experimental spectra at about -1 and -3 eV, respectively, while the calculated spectra exhibit only one peak at about -1 eV. Thus the broad structure at about -3 eV observed at the larger emission angles in the experimental spectra cannot be explained by direct bulk band transitions. The fact that the most severe discrepancy occurs at large emission angles indicates that disorder effects[18] may be of importance. Topographical disorder, such as surface roughness, naturally affects the conservation of the parallel component of the wave vector at the surface most severely at large emission angles, since the average distance a photoexcited electron travels through the surface region will increase with increasing emission angle. Hence, one would expect more density-of-states effects to occur at the larger emission angles. To investigate this further, in Fig. 8 we compare one of the Ar I–induced spectra, recorded at $\theta_i = 45°$ and $\theta_e = 72°$, with the corresponding calculated spectrum, and an XPS spectrum of ZrC measured by Ihara *et al.*[19] This figure clearly demonstrates that the structure at -3 eV in the experimental spectrum is mainly due to a three-dimensional density-of-states effect.

This observation justifies the remarks made earlier that effects caused by indirect transitions may contribute to the emission strength of peak *B* even at the smaller emission angles. In fact, it may explain the previously discussed dependence on the polarization of the radiation which is much weaker for peak *B* than for the other two peaks observed at normal emission in the experimental spectra.

B. The $\langle 011 \rangle$ azimuth

Angle-resolved EDC's from ZrC(100) measured at various emission angles along the $\langle 011 \rangle$ azimuth using unpolarized He I radiation are shown in Fig. 9. The incidence angle of the radiation is (a) $\theta_i = 17°$ and (b) $\theta_i = 45°$. As for the spectra recorded along the other azimuth, three distinct peaks are observed at normal emission. These peaks are labeled *A*, *B*, and *C* in accordance

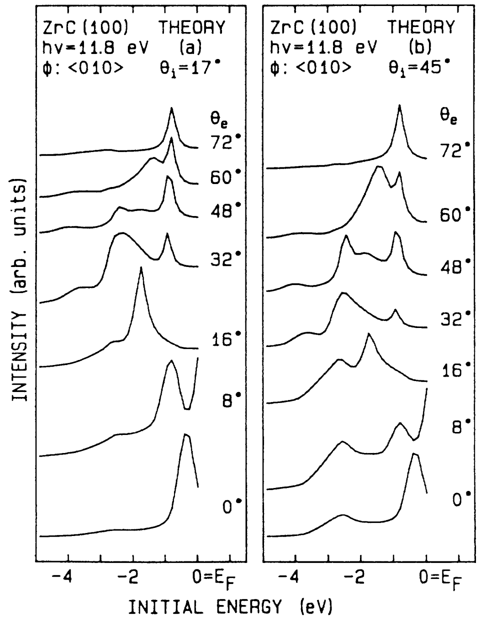

FIG. 7. Theoretical angle-resolved EDC's for ZrC(100) induced by 11.8-eV radiation and calculated at different emission angles along the $\langle 010 \rangle$ azimuth. The incidence angle of the radiation is (a) $\theta_i = 17°$ and (b) $\theta_i = 45°$.

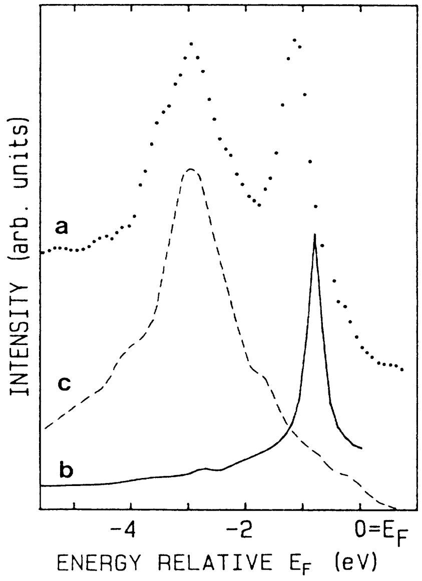

FIG. 8. Comparison between (a) the measured and (b) calculated Ar I–induced spectra at $\theta_i = 45°$ and $\theta_e = 72°$ along the $\langle 010 \rangle$ azimuth, and (c) the experimental XPS spectrum of ZrC by Ihara *et al.* (from Ref. 19).

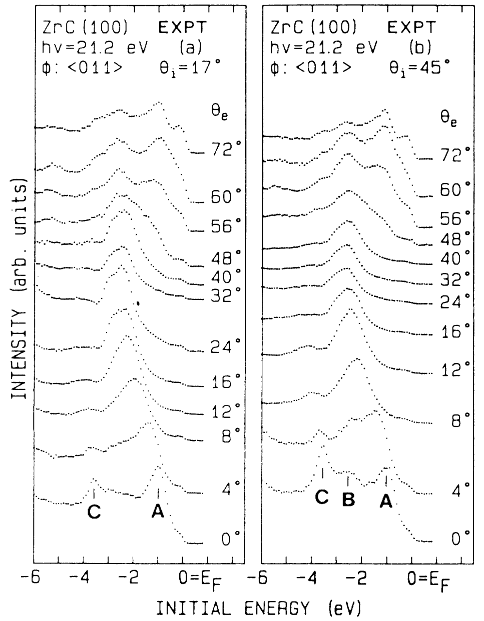

FIG. 9. Experimental angle-resolved EDC's for ZrC(100) using He I (21.2 eV) radiation and measured at various emission angles along the ⟨011⟩ azimuth. The incidence angle of the radiation is (a) $\theta_i = 17°$ and (b) $\theta_i = 45°$.

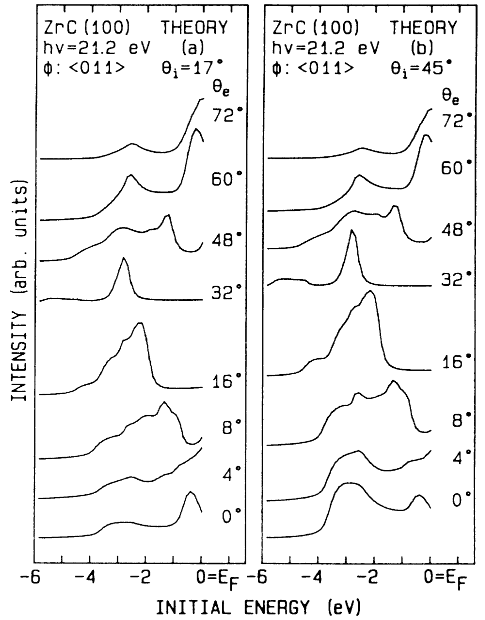

FIG. 10. Theoretical angle-resolved EDC's for ZrC(100) induced by 21.2-eV radiation and calculated at different emission angles along the ⟨011⟩ azimuth. The incidence angle of the radiation is (a) $\theta_i = 17°$ and (b) $\theta_i = 45°$.

with the previous notation. Again, the Δ_5 emission peak, *A*, is more intense at $\theta_i = 17°$, while peaks *B* and *C*, which are attributed to emission from states of Δ_1 symmetry, are significantly stronger at $\theta_i = 45°$. At the smaller emission angles, strong energy dispersions and intensity variations are observed for peaks *A* and *C*. Peak *A* shifts towards lower energies and becomes relatively stronger. Around $\theta_e = 8°$, peaks *A* and *B* start to overlap and merge into one structure. Peak *C* also moves downwards, but in contrast to peak *A*, it becomes weaker with increasing emission angles; it is hardly visible at $\theta_e > 20°$. At emission angles between $\theta_e = 20°$ and $\theta_e = 40°$, the spectra are essentially unaffected by the angle of emission, but at large emission angles, $\theta_e > 50°$, a new feature, which originates from the main structure at about -2.5 eV, appears. This feature moves towards the Fermi energy, exhibits an energy maximum at $\theta_e = 64°$, and shifts then back downwards again.

Theoretical angle-resolved EDC's for 21.2-eV radiation calculated at different emission angles along the ⟨011⟩ azimuth are shown in Fig. 10. The experimental incidence angles were used in the calculations, i.e., $\theta_i = 17°$ in Fig. 10(a) and $\theta_i = 45°$ in Fig. 10(b). The theoretical spectra are found to reproduce the experimental spectra fairly well; the experimental peak dispersions and relative peak intensities agree with the theoretical predictions. At normal emission, two structures of Δ_1 and Δ_5 symmetry appear. The Δ_1-derived peak shifts downwards and goes through an energy minimum at $\theta_e = 32°$, above which is it much weaker, thus reflecting the behavior of peak *C* in the experimental spectra quite well. Moreover, at $\theta_e = 4°$ and $\theta_e = 8°$, in particular, a peak originating from the Δ_1 structure comes up at about -2.5 eV. Keeping in mind that the analyzer has a finite angular resolution and actually is integrating over an acceptance cone with a semiangle of about 2°, these results suggest that direct transitions from the Δ_1 bulk band strongly contribute to the emission strength of peak *B* at small emission angles. Peak *A* in the experimental spectra is fairly well mimicked by the main Δ_5-derived peak, which rapidly shifts downwards and at $\theta_e = 32°$ dominates the spectra almost totally. At $\theta_e = 48°$, a strongly dispersing structure comes up at an energy slightly below -1 eV. It moves towards the Fermi energy and becomes more intense as the emission angle increases, in accordance with the experimental results. A minor difference in absolute peak locations is also found for this azimuth; the theoretical features are in general located about 0.5 eV closer to the Fermi energy.

Figure 11 shows EDC's recorded at different emission angles along the ⟨011⟩ azimuth using unpolarized Ne I radiation. Again, the polarization effects observed at normal emission allow the symmetry of peaks *A* and *C* to be identified as due to initial states of Δ_5 and Δ_1 symmetry, respectively. At this photon energy the emission strength of peak *B* is found to be much less affected by the polarization of the radiation. Moreover, a nondispersive feature appears at about -3 eV in most of the spectra measured at different emission angles, suggesting that peak *B* may be due to indirect transitions. It will, however, be shown below when comparing the experimental results with calculated spectra that direct transitions from the Δ_1-bulk initial-state band also contribute

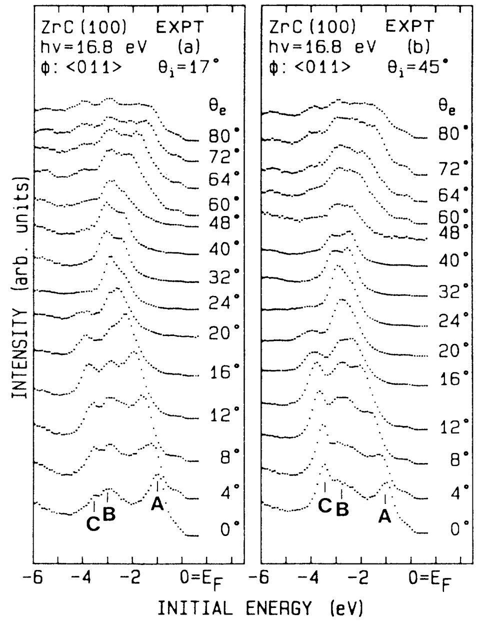

FIG. 11. Experimental angle-resolved EDC's from ZrC(100) using Ne I (16.8 eV) radiation and measured at various emission angles along the ⟨011⟩ azimuth. The incidence angle of the radiation is (a) $\theta_i = 17°$ and (b) $\theta_i = 45°$.

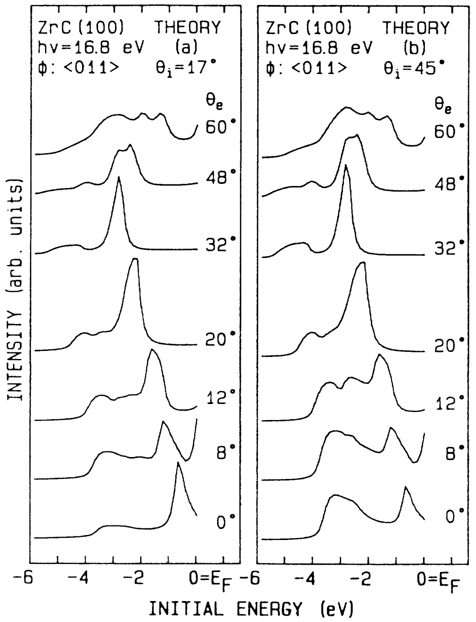

FIG. 12. Theoretical angle-resolved EDC's for ZrC(100) induced by 16.8-eV radiation and calculated at different emission angles along the ⟨011⟩ azimuth. The incidence angle of the radiation is (a) $\theta_i = 17°$ and (b) $\theta_i = 45°$.

strongly to the emission strength of this peak. The trends in the dispersions of peaks *A* and *C* resemble those observed in the He I–induced recorded spectra. Peak *A* moves towards peak *B*, from which it cannot be clearly resolved at $\theta_e = 20°$, and exhibits a shallow energy minimum around $\theta_e = 30°$. Peak *C* shifts downwards and dies out almost completely above $\theta_e = 30°$. At large emission angles, $\theta_e > 60°$, the main structure at -3 eV is seen to split into two peaks. The uppermost of these shifts rapidly towards higher energies, while the other remains located at about -3 eV. At these emission angles, a feature shifting slightly upwards can be observed around -4 eV.

Figure 12 shows angle-resolved spectra for 16.8-eV radiation calculated at various emission angles along the ⟨011⟩ azimuth. The experimental results are in good agreement with the theoretical spectra. The theoretical spectra show that the occurrence of three emission peaks at small emission angles is fairly well accounted for by direct bulk energy-band transitions. This is most easily seen in the spectrum calculated at $\theta_i = 45°$ and $\theta_e = 12°$, which clearly exhibits three distinct peaks. The two lower-lying peaks are derived from the broad Δ_1 structure at normal emission, thus reflecting the behavior of peaks *B* and *C* fairly well. In accordance with the experimental data, the main Δ_5-derived structure moves at the smaller emission angles systematically towards lower energies and gains relative strength. Moreover, at $\theta_e = 48°$, the main peak splits into a doublet structure, which together with the lowest lying (Δ_1-derived) peak gives rise to three emission features at $\theta_e = 60°$. The dispersion of the lowest-lying structure also agrees with that observed for peak *C* in the experimental spectra, but we note that since this peak is more intense in the theoretical spectra, the calculated energy dispersion is easier to follow, in particular at the larger emission angles.

Experimental EDC's were also recorded using unpolarized Ar I radiation. The results from these measurements are presented in Fig. 13. Calculated spectra corresponding to some of the experimental EDC's are shown in Fig. 14. In agreement with the results obtained along the ⟨010⟩ azimuth, two structures originating from initial states of Δ_1 and Δ_5 symmetry, respectively, appear in both the experimental and theoretical spectra. At this photon energy, almost no dispersion is observed for the Δ_1-derived structure, while the Δ_5-derived peak again moves systematically downwards. The agreement between the recorded and calculated spectra shows that the peaks observed in the experimental spectra are fairly well explained in terms of direct bulk energy-band transitions. In addition, the calculated spectra provide an explanation for the occurrence of a feature close to the Fermi energy observed at $\theta_e = 8°$ in the experimental spectra. The Δ_5 emission peak is, due to the lowering of symmetry when going off normal emission, in general, split into two peaks. One of these is seen to move towards the Fermi energy, while the other, which is more intense, gives rise to the main, downward-dispersing peak (see the calculated spectra at $\theta_i = 45°$ and $\theta_e = 8°$). Again, the theoretical spectra tend to locate the spectral features slightly closer to the Fermi energy, but there is a close resemblance between the experimental and theoretical peak dispersions. The relative intensities of the peaks observed in the experimental spectra are also fairly well mimicked by the calculations, although at $\theta_e = 20°$, the Δ_1-derived structure is

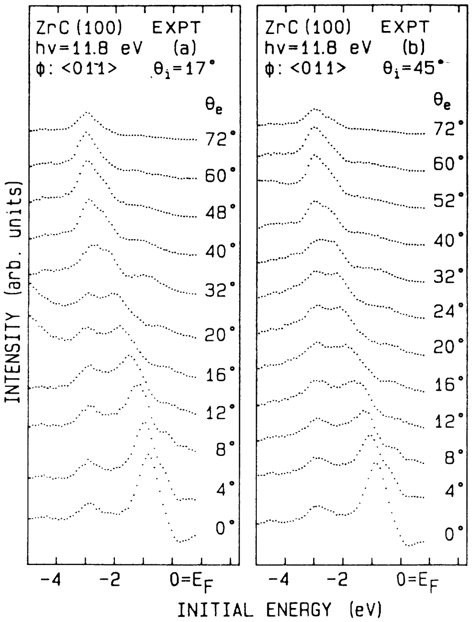

FIG. 13. Experimental angle-resolved EDC's from ZrC(100) using Ar I (11.8 eV) radiation and measured at various emission angles along the ⟨011⟩ azimuth. The incidence angle of the radiation is (a) $\theta_i = 17°$ and (b) $\theta_i = 45°$.

significantly weaker in the theoretical spectra. This may, however, be due to density-of-states effects, which are expected to contribute to the emission at -3 eV, at least at the larger emission angles, as was shown for the Ar I induced spectra recorded along the ⟨010⟩ azimuth. Interestingly, we see that the peak dispersions with the emission angle along the ⟨010⟩ and the ⟨011⟩ azimuths are quite different at large emission angles (compare Figs. 7 and 14).

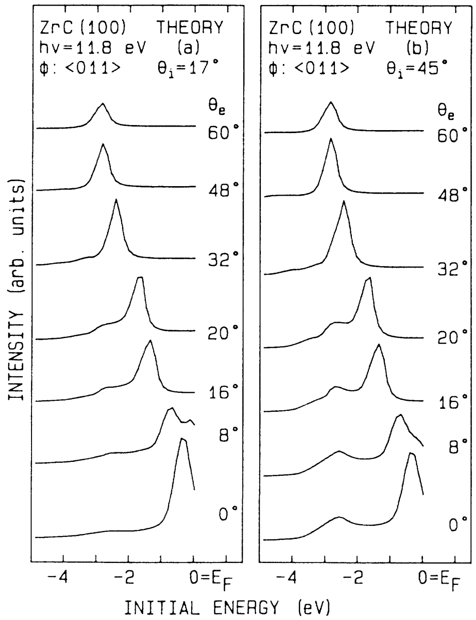

FIG. 14. Theoretical angle-resolved EDC's for ZrC(100) induced by 11.8-eV radiation and calculated at different emission angles along the ⟨011⟩ azimuth. The incidence angle of the radiation is (a) $\theta_i = 17°$ and (b) $\theta_i = 45°$.

C. Discussion

The comparison between the experimental and calculated spectra shows that most of the structures observed in the experimental spectra are due to direct bulk energy-band transitions. The results show that no structure in the recorded spectra should be associated with vacancy- or surface-induced states. A good agreement concerning peak dispersions and relative peak intensities was, in general, found. The absolute peak positions were, however, located slightly higher in the theoretical spectra. This difference in peak locations between the experimental and theoretical spectra is in accordance with previous photoemission studies of the transition-metal nitrides and carbides,[15–17] showing that the theoretically predicted energy positions are considerably higher, in particular for the Δ_5-derived peak. Apart from this, the most significant difference between the measured and calculated spectra concerns peak *B*, observed in the Ne I– and the He I–induced experimental spectra. This peak, which seems to exhibit Δ_1 symmetry in the He I–induced normal emission spectra, appears stronger in the measured spectra and shows almost no dispersion, indicating that it may be due to effects involving indirect transitions. However, the calculated spectra show a broad Δ_1 structure at normal emission, and moreover, in some of the spectra a clear shoulder appears on the high-energy side of the Δ_1 structure at normal emission. This shoulder is due to direct transitions from the steep part of the Δ_1 initial-state band (see Fig. 1), which also accounts for the large width of the Δ_1 structure. To illustrate this, in Fig. 15 the calculated energy-band structure along the $\Gamma \rightarrow X$ symmetry line is shown together with the final-state bands of Δ_1 symmetry that are utilized in the direct transitions. The final-state bands (dashed lines) have been displaced downwards by amounts corresponding to the photon energies used (11.8, 16.8, and 21.2 eV). Figure 15 shows that, while for Ne I (16.8 eV) and He I (21.2 eV) radiation a free-electron-like band serves as a final-state band for transitions from the Δ_1 initial-state band at normal emission, this is not the case for Ar I (11.8 eV) radiation. Remembering that the energy bands have an appreciable energy width, Fig. 15 shows that for He I radiation, in particular, and for Ne I radiation, direct transitions may take place from a large energy region of the steep parts of the Δ_1 initial-state band. Furthermore, since the probability of direct transitions from the steepest part of the Δ_1 initial-state band is expected to be high at $h\nu = 21.2$ eV, Fig. 15 also shows why peak *B* exhibits its strongest dependence on the incidence angle of the radiation for He I radiation.

It should be pointed out that the finite angular resolution of the analyzer may explain why peak *B* is more intense in the experimental spectra. Since the analyzer is integrating over an acceptance cone with a semiangle of 2°, electrons leaving the surface with a nonvanishing

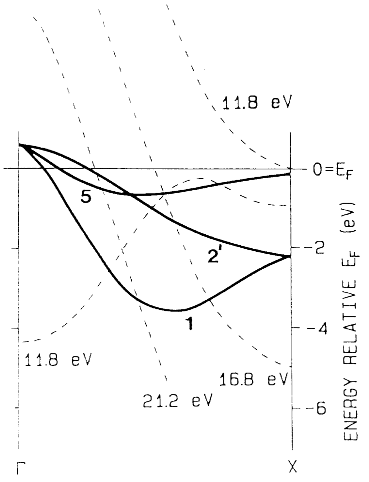

FIG. 15. Calculated energy-band structure of $ZrC_{1.0}$ along the $\Gamma \rightarrow X$ symmetry line. The dashed lines show the final-states bands used in the direct transitions for He I, Ne I, and Ar I radiation, displaced downwards by the amounts indicated. See text for details.

parallel component of the wave vector will contribute to the photocurrent detected at normal emission. In fact, some of the calculated spectra show that a distinct peak comes up at about -2.5 eV in the spectra calculated a few degrees off normal emission. Hence, there are evidently direct bulk band transitions that may contribute to the emission strength of peak *B*, at least close to normal emission.

The Ar I induced experimental spectra recorded along the $\langle 010 \rangle$ azimuth show, however, that a structure reflecting the three-dimensional density of states appears at large emission angles. Since this feature is located at about -3 eV, we cannot exclude that three-dimensional density-of-states effects may be present even at the smaller emission angles. In this context, it is interesting to note that the Ar I–induced spectra along the $\langle 011 \rangle$ azimuth do not allow the structure at about -3 eV, appearing at large emission angles in the measured spectra, to be attributed solely to a density-of-states effect, since the main Δ_5-derived structure is located at about the same energy (compare Figs. 7 and 14). It is also worth mentioning that, since the flat part of the Δ_1 initial-state band at the *X* point of the $\Gamma \rightarrow X$ symmetry line is located at about -2.3 eV, we cannot rule out that also one-dimensional density-of-states effects may contribute to the emission intensity of peak *B*. One-dimensional density-of-states effects, reflecting the flat part of the Δ_1 initial-state band, have been observed previously on other transition-metal carbides and nitrides and tend to show strong dependence on the polarization of the radiation.[17,20]

Qualitatively, the band structure in Fig. 15 also explains why the relative intensity ratio between the Δ_5 and the Δ_1 emission peaks is much larger for 11.8-eV radiation than for the other two photon energies used. At $h\nu = 11.8$ eV, direct transitions from the Δ_5 initial-state band may occur close to the *X* point at the Brillouin zone boundary, at which both the initial-state band and the free-electron-like final-state band have a high density of states. As a result, direct transitions are allowed at a maximum in the joint density of states, and consequently the transition probability is expected to be high.

We would like to conclude these remarks by pointing out some differences between the spectra obtained along the two azimuthal directions. Since the calculated spectra tend to exhibit sharper structures and only take account of direct bulk band transitions, we concentrate on these in the comparison between the two azimuths. In general, the spectra are fairly similar close to normal emission, as one would expect, but at large emission angles the difference between the two azimuthal directions becomes clear. Along the $\langle 011 \rangle$ azimuth the lowest lying Δ_1-derived structure shows stronger dispersion and exhibits a deep energy minimum around $\theta_e = 30°$. In contrast to the spectra obtained along the $\langle 011 \rangle$ azimuth, a sharp peak appears around -1 eV at $\theta_e > 30°$ in the spectra obtained along the $\langle 010 \rangle$ azimuth, as is most easily seen in the Ne I–induced spectra. The most obvious difference occurs, however, when comparing the calculated Ar I–induced spectra. Along the $\langle 011 \rangle$ azimuth the main Δ_5-derived structure moves monotonically towards lower energies, while along the $\langle 010 \rangle$ azimuth it reverses its direction of dispersion at about $\theta_e = 48°$ and moves rapidly back towards the Fermi energy.

IV. SUMMARY

The electronic band structure of ZrC(100) has been investigated using angle-resolved photoelectron spectroscopy. Energy distribution curves were recorded with the electron emission directed along the $\langle 010 \rangle$ and the $\langle 011 \rangle$ symmetry directions utilizing unpolarized He I, Ne I, and Ar I radiation. The band structure of $ZrC_{1.0}$, calculated using the linear augmented-plane-wave method, was used for interpreting the normal-emission data. The recorded spectra were also compared with calculated angle-resolved spectra for $ZrC_{1.0}(100)$. The results showed that most of the peaks observed in the experimental spectra are due to direct bulk energy-band transitions. The calculated spectra were found to reproduce the experimental peak dispersions and peak intensity variations remarkably well, which firmly shows the applicability of the extended version of Pendry's model for calculating the photocurrent from binary compounds. A nondispersive structure observed at large emission angles in the Ar I–induced measured spectra was attributed to a three-dimensional density-of-states effect, from a comparison with an earlier measured XPS spectrum of ZrC.[19]

ACKNOWLEDGMENTS

The authors wish to thank Dr. P. E. S. Persson for providing the LAPW programs used in the band-structure calculations, and for valuable discussions. The financial support from the Swedish Natural Science Research Council is also gratefully acknowledged.

[1] L. E. Toth, *Transition Metal Carbides and Nitrides* (Academic, New York, 1971).

[2] C. G. Larsson, thesis, Chalmers University of Technology, Gothenburg, 1982 (ISBN 91-7032-078-0).

[3] J. F. L. Hopkinson, J. B. Pendry, and D. J. Titterington, Comput. Phys. Commun. **19**, 69 (1980).

[4] A. N. Christensen, J. Crystal Growth **33**, 99 (1976).

[5] The chemical analysis of the crystal was made at AB Sandvik Hard Materials, Box 42056, S-12612 Stockholm, Sweden.

[6] O. K. Andersen, Phys. Rev. B **12**, 3060 (1975).

[7] D. J. Chadi and M. L. Cohen, Phys. Rev. B **8**, 5747 (1973).

[8] P. Hohenberg and W. Kohn, Phys. Rev. **136**, B864 (1964).

[9] L. Hedin and B. I. Lundquist, J. Phys. C **4**, 2064 (1971).

[10] P. Weinberger, Ber. Bunsenges. Phys. Chem. **81**, 804 (1977).

[11] L. I. Johansson, C. G. Larsson, and A. Callanås, J. Phys. F **14**, 1761 (1984).

[12] C. G. Larsson, L. I. Johansson, and A. Callenås, Solid State Commun. **49**, 727 (1984).

[13] J. Hermanson, Solid State Commun. **22**, 9 (1977).

[14] W. Eberhardt and F. J. Himpsel, Phys. Rev. B **21**, 5572 (1980).

[15] L. I. Johansson, A. Callenås, P. M. Stefan, A. N. Christensen, and K. Schwarz, Phys. Rev. B **24**, 1883 (1981).

[16] A. Callenås, L. I. Johansson, A. N. Christensen, K. Schwarz, P. Blaha, and J. Redinger, Phys. Rev. B **30**, 635 (1984).

[17] A. Callenås, L. I. Johansson, A. N. Christensen, K. Schwarz, and P. Blaha, Phys. Rev. B **32**, 575 (1985).

[18] N. J. Shevchik, Phys. Rev. B **16**, 3428 (1977).

[19] H. Ihara, M. Hirabayashi, and H. Nakagawa, Phys. Rev. B **14**, 1707 (1976).

[20] P. A. P. Lindberg, L. I. Johansson, J. B. Lindström, P. E. S. Persson, D. S. L. Law, and A. N. Christensen, Phys. Rev. B (to be published).